Computing limit loads by minimizing a sum of norms

Knud D. Andersen* Edmund Christiansen† Michael L. Overton‡

October 17, 1994

Abstract

This paper treats the problem of computing the collapse state in limit analysis for a solid with a quadratic yield condition, such as, for example, the Mises condition. After discretization with the finite element method, using divergence-free elements for the plastic flow, the kinematic formulation turns into the problem of minimizing a sum of Euclidean vector norms, subject to a single linear constraint. This is a nonsmooth minimization problem, since many of the norms in the sum may vanish at the optimal point. However, efficient solution algorithms for this particular convex optimization problem have recently been developed.

The method is applied to test problems in limit analysis in two different plane models: plane strain and plates. In the first case more than 80 percent of the terms in the sum are zero in the optimal solution, causing severe ill-conditioning. In the last case all terms are nonzero. In both cases the algorithm works very well, and problems are solved which are larger by at least an order of magnitude than previously reported. The relative accuracy for the solution of the discrete problems, measured by duality gap and feasibility, is typically of the order 10^{-8}. The discretization error, due to the finite grid, depends on the nature of the solution. In the applications reported here it ranges from 10^{-5} to 10^{-2}.

Keywords: Limit analysis, plasticity, finite element method, nonsmooth optimization.

AMS(MOS) subject classification: 65K10, 65N30, 73E20, 90C06, 90C25, 90C90.

Abbreviated title: Computing limit loads

The authors are grateful to Ken Kortanek for suggesting this collaboration.

*Odense University. Supported by the Danish Science Research Council

†Odense University

‡Courant Institute of Mathematical Sciences, New York University. Supported in part by the U.S. National Science Foundation

1 Introduction

The problem of limit analysis is the following: Given a load distribution on a rigid plastic solid, what is the maximum multiple of this load that the solid can sustain without collapsing? And when collapse does occur, what are the fields of stresses and plastic flow in the collapse state? In particular it is of interest to find the *plastified region*, where the stresses are at the yield surface and where plastic deformation takes place. It is harder to find the collapse fields than the collapse multiplier. In typical cases these fields are not uniquely determined, in contrast to the equilibrium problems within the elastic model.

We shall use the following notation:

V	:	domain occupied by the solid
S	:	fixed part of V's surface
T	:	free and possibly loaded part of the surface
$\boldsymbol{f} = \boldsymbol{f}(\boldsymbol{x})$	:	volume force at $\boldsymbol{x} \in V$
$\boldsymbol{g} = \boldsymbol{g}(\boldsymbol{x})$	:	surface force at $\boldsymbol{x} \in T$
$\boldsymbol{\sigma} = (\sigma_{ij})$	:	stress tensor (symmetric)
$\boldsymbol{\sigma} \in \mathcal{K}$	:	the yield condition
$\boldsymbol{u} = (u_i)$	:	plastic flow field
$\boldsymbol{\varepsilon} = (\varepsilon_{ij})$	:	plastic deformation rate tensor defined by

$$\varepsilon_{ij} = \frac{1}{2}\left(\frac{\partial u_i}{\partial x_j} + \frac{\partial u_j}{\partial x_i}\right) \tag{1}$$

The work rate for the pair of forces $(\boldsymbol{f}, \boldsymbol{g})$ and a virtual plastic flow $\boldsymbol{u}$ is

$$F(\boldsymbol{u}) = \int_V \boldsymbol{f} \cdot \boldsymbol{u} + \int_T \boldsymbol{g} \cdot \boldsymbol{u}. \tag{2}$$

The work rate for the internal stresses is given by the bilinear form

$$a(\boldsymbol{\sigma}, \boldsymbol{u}) = \int_V \sum_{i,j} \sigma_{ij}\varepsilon_{ij} d\boldsymbol{x} = \int_V \sum_{i,j} \sigma_{ij} \frac{\partial u_i}{\partial x_j} d\boldsymbol{x} \tag{3}$$

$$= -\int_V (\nabla \cdot \boldsymbol{\sigma}) \cdot \boldsymbol{u}\ dx + \int_T (\boldsymbol{\nu} \cdot \boldsymbol{\sigma}) \cdot \boldsymbol{u}\ ds \tag{4}$$

where $\boldsymbol{\nu}$ denotes the outward normal to V. The equality between (3) and (4) follows from Green's formula using that $\boldsymbol{u} = \boldsymbol{0}$ on S.

The equilibrium equation for $\boldsymbol{\sigma}$ is the equation of virtual work rate:

$$a(\boldsymbol{\sigma}, \boldsymbol{u}) = F(\boldsymbol{u}) \quad \text{for all} \quad \boldsymbol{u} \quad \text{with} \quad \boldsymbol{u} = \boldsymbol{0} \quad \text{on} \quad S. \tag{5}$$

Comparing (2) and (4) we see that (5) is equivalent to the classical form of the equilibrium equation:

$$-\nabla \cdot \boldsymbol{\sigma} = \boldsymbol{f} \quad \text{in} \quad V, \quad \boldsymbol{\nu} \cdot \boldsymbol{\sigma} = \boldsymbol{g} \quad \text{on} \quad T.$$

For computational purposes we shall always use the form (3).

In this paper we assume that the yield condition is of the form

$$\boldsymbol{\sigma} \in \mathcal{K} \Leftrightarrow K(\boldsymbol{\sigma}) \leq 1 \tag{6}$$

where K is a quadratic function in the components of $\boldsymbol{\sigma}$. For example the Mises condition is

$$(\sigma_{11} - \sigma_{22})^2 + (\sigma_{22} - \sigma_{33})^2 + (\sigma_{33} - \sigma_{11})^2 + 6(\sigma_{12}^2 + \sigma_{23}^2 + \sigma_{31}^2) \leq 2\sigma_0^2 \tag{7}$$

σ_0 being the yield stress in simple tension. The yield condition must be satisfied at every point in the solid. Note that (7) does not put a bound on the diagonal components of $\boldsymbol{\sigma}$. For simplicity of notation we have assumed that the material is homogeneous, and that the boundary condition on $\boldsymbol{u}$ is of the simple type above.

The limit multiplier λ^* is given by (Christiansen [10, 14])

$$\begin{aligned}
\lambda^* &= \max\{\lambda \mid \exists\, \boldsymbol{\sigma} \in \mathcal{K} : a(\boldsymbol{\sigma}, \boldsymbol{u}) = \lambda F(\boldsymbol{u}) \quad \forall\, \boldsymbol{u}\} && (8)\\
&= \max_{\sigma \in \mathcal{K}} \min_{F(u)=1} a(\boldsymbol{\sigma}, \boldsymbol{u}) && (9)\\
&= \min_{F(u)=1} \max_{\sigma \in \mathcal{K}} a(\boldsymbol{\sigma}, \boldsymbol{u}) && (10)\\
&= \min_{F(u)=1} D(\boldsymbol{u}) && (11)
\end{aligned}$$

where

$$D(\boldsymbol{u}) = \max_{\sigma \in \mathcal{K}} a(\boldsymbol{\sigma}, \boldsymbol{u}). \tag{12}$$

The expression (8) states the existence of an admissible stress tensor $\boldsymbol{\sigma} \in \mathcal{K}$ which is in equilibrium with the external forces $(\lambda \boldsymbol{f}, \lambda \boldsymbol{g})$. (9) follows from simple linear algebra, while (10) is the duality theorem of limit analysis proved in [12] and [14, Section 5]. The expressions (8) and (11) are traditionally known respectively as the static and kinematic principles of limit analysis.

The solution to the problem of limit analysis consists of the triple $(\lambda^*, \boldsymbol{\sigma}^*, \boldsymbol{u}^*)$, where $(\boldsymbol{\sigma}^*, \boldsymbol{u}^*)$ is a saddle point for (9)–(10). $\boldsymbol{\sigma}^*$ and $\boldsymbol{u}^*$ are then fields of stress and flow in the

collapse state. It follows from the kinematic principle (11) that

$$\lambda^* = a(\boldsymbol{\sigma}^*, \boldsymbol{u}^*) = D(\boldsymbol{u}^*) = \max_{\sigma \in \mathcal{K}} a(\boldsymbol{\sigma}, \boldsymbol{u}^*).$$

Inserting the form (3) for $a(\boldsymbol{\sigma}, \boldsymbol{u})$ we get

$$\int_V \sum_{i,j} \sigma_{ij}^* \, \varepsilon_{ij}(\boldsymbol{u}^*) \, d\boldsymbol{x} = \max_{\sigma \in \mathcal{K}} \int_V \sum_{i,j} \sigma_{ij} \, \varepsilon_{ij}(\boldsymbol{u}^*) \, dx$$

which leads to the principle of complimentary slackness in limit analysis: At each point in the material where $\boldsymbol{\varepsilon}(\boldsymbol{u}^*)$ is nonzero, the collapse stress tensor $\boldsymbol{\sigma}^*$ must be at the yield surface at a point with $\boldsymbol{\varepsilon}(\boldsymbol{u}^*)$ as the outward normal. Regions with $\boldsymbol{\varepsilon}(\boldsymbol{u}^*) = \mathbf{0}$ are rigid. Points where $\boldsymbol{\varepsilon}(\boldsymbol{u}^*) \neq \mathbf{0}$, implying that $\boldsymbol{\sigma}^*$ is at the yield surface, belong to the *plastified region*. Identification of these regions is an important part of the solution process.

The Mises yield condition (7) is insensitive to the addition of any tensor of the form $\varphi \boldsymbol{I}$, where $\boldsymbol{I} = (\delta_{ij})$ is the unit tensor. This reflects the property that purely hydrostatic pressure (or underpressure) does not affect plastic collapse. We assume that the set $\mathcal{K}$ of admissible tensors in condition (6) is either bounded (the easy case) or of the type discussed above:

$$\boldsymbol{\sigma} \in \mathcal{K} \Leftrightarrow (\boldsymbol{\sigma} - \varphi \boldsymbol{I}) \in \mathcal{K} \quad \text{for any function} \quad \varphi. \tag{13}$$

The case where $\mathcal{K}$ is bounded occurs in the plane stress model and in the plate model. The unbounded case occurs in 3–dimensional problems and in the plane strain model. We concentrate on the unbounded case, although we shall report computational results for the plate model as well.

Assume now that the yield condition satisfies (13). Then it is easy to see that the so–called energy dissipation rate $D(\boldsymbol{u})$ defined by (12) is finite if and only if $\boldsymbol{u}$ is divergence free, $\nabla \cdot \boldsymbol{u} = 0$, i.e. the plastic flow is incompressible. This condition is an infinite set of linear constraints on $\boldsymbol{u}$ in the minimization problem (11). For this reason the standard approach in limit analysis with unbounded yield set has been to solve the discrete form of the maximization problem (8). This problem is large, sparse and ill–conditioned, partially due to the unbounded feasible set. Since efficient convex programming methods for such problems were not available, the yield condition was linearized, and the resulting linear program (LP) was solved with the simplex method (see e.g. [2, 7, 10]).

In [15] and [16] it was demonstrated that interior-point LP methods are very competitive in limit analysis making it possible to solve for finer grids. Also interior-point methods give more "physically correct" collapse fields than the extreme point principle of the simplex method: in the typical case of non-unique or poorly determined solutions an

extreme point method may pick a solution which oscillates from node to node. During the 1980's efficient convex programming methods appeared, such as MINOS (Murtagh and Saunders [23]). Application of MINOS to limit analysis was reported in [13] and [14]: the limit multiplier is more accurately determined without linearization of constraints, but the collapse fields display unphysical fluctuations due to the extreme point nature of the algorithm in MINOS. (For many problems this extreme point nature of the algorithm is desirable, but not in continuum mechanics.)

A new and very efficient infeasible point method for linear programming by Andersen [3] was applied to limit analysis in [5] (also reported in [14]). Problems one order of magnitude larger than before were solved. The purpose of this paper is to present a convex programming method for limit analysis with similar efficiency.

In the case where the set $\mathcal{K}$ of admissible stress tensors is bounded, the collapse problem has been solved by minimizing a sum of norms in [25] (antiplane shear) and in [21] (plane stress). Compared with these applications we emphasize the following differencies in the present work:

- Handling unbounded yield set.
- Using mixed finite element methods.
- Using a more efficient method to minimize the sum of norms.
- Solving both larger and more ill-conditioned problems than previously possible.

2 The method

We assume that the yield condition is of the form (13) and impose the implicit constraint $\nabla \cdot \boldsymbol{u} = 0$. Then

$$a(\varphi \boldsymbol{I}, \boldsymbol{u}) = \int_V \varphi(\nabla \cdot \boldsymbol{u}) d\boldsymbol{x} = 0$$

for all scalar functions φ. Hence we need only consider stress tensors satisfying $\sum \sigma_{ii} = 0$ in the duality problem (8)–(11). With this restriction the set of admissible tensors is bounded, and hence the objective function $D(\boldsymbol{u})$ in the minimization problem (11) is finite for all $\boldsymbol{u}$ satisfying $\nabla \cdot \boldsymbol{u} = 0$. The details are given in [12] and in [14, Section 5.4].

Using standard finite element spaces it is straightforward to find a discrete representation for stresses satisfying $\sum \sigma_{ii} = 0$ and thus reduce the problem size. The constraint $\nabla \cdot \boldsymbol{u} = 0$ is a complication known from finite element computations in fluid mechanics,

discussed in e.g. Temam [26, Section 4.4–4.5]. The trick is to represent the flow $\boldsymbol{u}$ as a curl, $\boldsymbol{u} = \nabla \times \Psi$, which implies $\nabla \cdot \boldsymbol{u} = 0$. Instead of choosing finite elements for the flow $\boldsymbol{u}$ itself we discretize the vector Ψ to a finite element representation Ψ_h, such that the discrete flow $\boldsymbol{u}_h$ is given by

$$\boldsymbol{u}_h = \nabla \times \Psi_h. \tag{14}$$

(h is a linear measure of the element size in the discretization.) Care must be taken to ensure that $\boldsymbol{u}_h$ satisfies the boundary conditions.

This way we obtain not only a finite and computable objective function $D(\boldsymbol{u})$ for the minimization problem (11); we also get a reduction in problem size by removing compressible flow and purely hydrostatic pressure from the duality problem. There is a price to pay, though: The discrete flow $\boldsymbol{u}_h$ must be continuous because of the boundary condition and the derivatives in the expression (3). Hence Ψ_h must be of class C^1. In two space dimensions this implies the use of elements like the Argyris triangle or the Bell triangle. If the geometry permits a triangulation into rectangles (in two or three space dimensions), then the tensor product of the standard cubic C^1–elements (Bogner–Fox–Schmit rectangle) is a convenient choice. (All these finite elements are described in Ciarlet [19, Section 2.2] and [20, Section 9].)

In plane strain this approach is particularly attractive: Ψ_h only has one nonzero component which we shall denote Ψ_h, and equation (14) reduces to

$$\boldsymbol{u}_h = \left(\frac{\partial \Psi_h}{\partial x_2} \, , \, - \frac{\partial \Psi_h}{\partial x_1} \right). \tag{15}$$

The corresponding stress tensor of trace zero satisfies $\sigma_{22} = -\sigma_{11}$ and may be identified with the vector (σ_1, σ_2), where

$$\boldsymbol{\sigma}_h = \begin{bmatrix} \sigma_1 & \sigma_2 \\ \sigma_2 & -\sigma_1 \end{bmatrix} \tag{16}$$

With this notation the Mises yield condition in plane strain becomes

$$\sigma_1^2 + \sigma_2^2 \leq \frac{1}{3}\sigma_0^2. \tag{17}$$

In order to be specific we proceed to describe the discretization of the plane strain case with bi–cubic C^1–elements over rectangles (the Bogner–Fox–Schmit rectangle) for Ψ_h. The nodes for this finite element space are the vertices of the rectangles. There are four basis functions associated with each vertex μ, corresponding to the following nodal values of Ψ_h ([20, page 92]):

$$\Psi \, , \, \frac{\partial \Psi}{\partial x_1} \, , \, \frac{\partial \Psi}{\partial x_2} \, , \, \frac{\partial^2 \Psi}{\partial x_1 \partial x_2}.$$

The corresponding four basis functions are denoted ψ_μ^{00}, ψ_μ^{10}, ψ_μ^{01}, ψ_μ^{11}. If V_μ denotes an arbitrary vertex, then $\psi_\mu^{\alpha\beta}$ is completely characterized by the following identities:

$$\begin{aligned}
&\psi_\mu^{00}(V_\nu) = \delta_{\mu\nu}\ , \quad \frac{\partial}{\partial x_1}\psi_\mu^{00}(V_\nu) = 0\ , \quad \frac{\partial}{\partial x_2}\psi_\mu^{00}(V_\nu) = 0\ , \quad \frac{\partial^2}{\partial x_1 \partial x_2}\psi_\mu^{00}(V_\nu) = 0\\
&\psi_\mu^{10}(V_\nu) = 0\ , \quad \frac{\partial}{\partial x_1}\psi_\mu^{10}(V_\nu) = \delta_{\mu\nu}\ , \quad \frac{\partial}{\partial x_2}\psi_\mu^{10}(V_\nu) = 0\ , \quad \frac{\partial^2}{\partial x_1 \partial x_2}\psi_\mu^{10}(V_\nu) = 0\\
&\psi_\mu^{01}(V_\nu) = 0\ , \quad \frac{\partial}{\partial x_1}\psi_\mu^{01}(V_\nu) = 0\ , \quad \frac{\partial}{\partial x_2}\psi_\mu^{01}(V_\nu) = \delta_{\mu\nu}\ , \quad \frac{\partial^2}{\partial x_1 \partial x_2}\psi_\mu^{01}(V_\nu) = 0\\
&\psi_\mu^{11}(V_\nu) = 0\ , \quad \frac{\partial}{\partial x_1}\psi_\mu^{11}(V_\nu) = 0\ , \quad \frac{\partial}{\partial x_2}\psi_\mu^{11}(V_\nu) = 0\ , \quad \frac{\partial^2}{\partial x_1 \partial x_2}\psi_\mu^{11}(V_\nu) = \delta_{\mu\nu}
\end{aligned}$$

$\boldsymbol{\Psi}_h$ may now be written

$$\boldsymbol{\Psi}_h = \sum_\mu \sum_{\alpha=0}^{1} \sum_{\beta=0}^{1} \eta_\mu^{\alpha\beta}\ \psi_\mu^{\alpha\beta}. \tag{18}$$

The values of $\boldsymbol{u}_h$ at the vertices are determined by (15) and (18):

$$\boldsymbol{u}_h(V_\mu) = \left(\eta_\mu^{01},\ -\eta_\mu^{10}\right).$$

We now turn to the choice of finite element space for the stress components σ_1 and σ_2 in (16). There are no boundary conditions on the stresses and no derivatives on $\boldsymbol{\sigma}$ in the expression (3) for $a(\boldsymbol{\sigma}, \boldsymbol{u})$, so the discrete stresses need not even be continuous. However, as we shall explain below, the dimension of the space of discrete stresses $\boldsymbol{\sigma}_h$ must satisfy a compatibility condition with the dimension of the space for $\boldsymbol{\Psi}_h$ which in this case has four degrees of freedom per vertex. The space of piecewise bilinear functions is too small, but the space of piecewise bi-quadratic element functions satisfies this condition. The nodes are the vertices of the rectangles, the midpoints of the sides and the midpoint of the rectangles (see [20, page77]. Associated with each node N_ν there is a scalar basis function φ_ν characterized completely by being equal to one at this node and equal to zero at all other nodes. Consequently there are the following two basis functions for the space of discrete stresses $\boldsymbol{\sigma}_h$ given by (16):

$$\boldsymbol{\varphi}_\nu^1 = \begin{bmatrix} \varphi_\nu & 0 \\ 0 & -\varphi_\nu \end{bmatrix}\ , \quad \boldsymbol{\varphi}_\nu^2 = \begin{bmatrix} 0 & \varphi_\nu \\ \varphi_\nu & 0 \end{bmatrix}.$$

The discrete stress tensor may now be written

$$\boldsymbol{\sigma}_h = \sum_\nu \left(\xi_\nu^1 \boldsymbol{\varphi}_\nu^1 + \xi_\nu^1 \boldsymbol{\varphi}_\nu^2\right) \tag{19}$$

The yield condition (17) is imposed on the nodal values as follows

$$\left(\xi_\nu^1\right)^2 + \left(\xi_\nu^2\right)^2 \le \frac{1}{3}\sigma_0^2 \quad \text{for all nodes} \quad \nu. \tag{20}$$

After insertion of (18) and (19) into the expressions (2) and (3) the energy functions may be expressed as

$$F\left(\boldsymbol{u}_h\right) = \sum_{\mu} \sum_{\alpha=0}^{1} \sum_{\beta=0}^{1} \eta_{\mu}^{\alpha\beta} \, F_{\mu}^{\alpha\beta} \tag{21}$$

where

$$F_{\mu}^{\alpha\beta} = \int_V \left(f_1 \frac{\partial}{\partial x_2} \psi_{\mu}^{\alpha\beta} - f_2 \frac{\partial}{\partial x_1} \psi_{\mu}^{\alpha\beta} \right) d\boldsymbol{x} + \int_T \left(g_1 \frac{\partial}{\partial x_2} \psi_{\mu}^{\alpha\beta} - g_2 \frac{\partial}{\partial x_1} \psi_{\mu}^{\alpha\beta} \right) ds \tag{22}$$

and

$$a\left(\boldsymbol{\sigma}_h, \boldsymbol{u}_h\right) = \sum_{\nu} \sum_{k=1}^{2} \sum_{\mu} \sum_{\alpha=0}^{1} \sum_{\beta=0}^{1} \xi_{\nu}^{k} \eta_{\mu}^{\alpha\beta} A_{\nu\mu}^{k\alpha\beta}, \tag{23}$$

where

$$A_{\nu\mu}^{1\alpha\beta} = 2 \int_V \varphi_{\nu} \frac{\partial^2}{\partial x_1 \partial x_2} \psi_{\mu}^{\alpha\beta} \, d\boldsymbol{x} \tag{24}$$

$$A_{\nu\mu}^{2\alpha\beta} = \int_V \varphi_{\nu} \left(\frac{\partial^2}{\partial x_2^2} - \frac{\partial^2}{\partial x_1^2} \right) \psi_{\mu}^{\alpha\beta} \, d\boldsymbol{x}. \tag{25}$$

$F(\boldsymbol{u}_h)$ is a linear form and $a(\boldsymbol{\sigma}_h, \boldsymbol{u}_h)$ a bilinear form in the "long vectors" $\left(\xi_{\nu}^{k}\right)$ and $\left(\eta_{\mu}^{\alpha\beta}\right)$. This means that F corresponds to a vector and a to a matrix. It is necessary, at least for the classical algorithms of numerical linear algebra, that the coordinates of these vectors are given by one–dimensional numberings. These numberings are defined by one–to–one mappings

$$\begin{aligned} n &= n(\nu, k) \in \{1, 2, \cdots, N\} \\ m &= m(\mu, \alpha, \beta) \in \{1, 2, \cdots, M\}. \end{aligned}$$

Given these numberings the nodal values for $\boldsymbol{\sigma}_h$ and $\boldsymbol{u}_h$ may be written as "ordinary" vectors:

$$x_n = \xi_{\nu}^{k} \quad \text{where} \quad n = n(\nu, k) \tag{26}$$

$$y_m = \eta_{\mu}^{\alpha\beta} \quad \text{where} \quad m = m(\mu, \alpha, \beta). \tag{27}$$

The vectors $\boldsymbol{x} = (x_n)_{n=1}^{N} \in \mathbb{R}^N$ and $\boldsymbol{y} = (y_m)_{m=1}^{M} \in \mathbb{R}^M$ are in unique correspondence with the discrete fields $\boldsymbol{\sigma}_h$ and $\boldsymbol{u}_h$, respectively. Inserting these numberings into (21) and (23) we get:

$$F\left(\boldsymbol{u}_h\right) = \sum_{m=1}^{M} y_m b_m = \boldsymbol{b}^T \boldsymbol{y}, \tag{28}$$

where

$$b_m = F_{\mu}^{\alpha\beta} \, , \quad m = m(\mu, \alpha, \beta)$$

and

$$a(\boldsymbol{\sigma}_h, \boldsymbol{u}_h) = \sum_{m=1}^{M} \sum_{n=1}^{N} y_m x_n a_{mn} = \boldsymbol{y}^T \boldsymbol{A} \boldsymbol{x} = \boldsymbol{x}^T \left(\boldsymbol{A}^T \boldsymbol{y} \right). \tag{29}$$

$\boldsymbol{A}$ is the $M \times N$ matrix with entries

$$a_{mn} = A_{\nu\mu}^{k\alpha\beta}, \quad m = m(\mu, \alpha, \beta), \quad n = n(\nu, k).$$

The numberings $m(\mu, \alpha, \beta)$ and $n(\nu, k)$ are chosen in order to obtain a certain matrix structure in $\boldsymbol{A}$, typically to minimize fill–in during factorization.

With the present choice of finite element spaces, bi–quadratic for $\boldsymbol{\sigma}_h$ and bi–cubic for Ψ_h, the integrals in (22), (24) and (25) can be computed as products of one–dimensional integrals. Each integral is simple, but there are numerous different combinations. We found it advantageous to use a program for symbolic integration to compute these integrals as functions of the mesh size h.

We discretize the problem (8)–(12) by restricting $\boldsymbol{\sigma}$ and $\boldsymbol{u}$ to the finite dimensional spaces spanned by $\boldsymbol{\sigma}_h$ and $\boldsymbol{u}_h$ defined by our finite element functions. With the notation (28) and (29) we get a finite dimensional duality problem in the variables $\boldsymbol{x} \in \mathbb{R}^N$ and $\boldsymbol{y} \in \mathbb{R}^M$. Let $\mathcal{K}_d$ denote the set of $\boldsymbol{x} \in \mathbb{R}^N$ for which the corresponding (ξ_ν^k) satisfies the yield condition (20), and define

$$D_d(\boldsymbol{y}) = \max_{\boldsymbol{x} \in \mathcal{K}_d} \boldsymbol{x}^T (\boldsymbol{A}^T \boldsymbol{y}). \tag{30}$$

With this notation we get:

$$\begin{aligned}
\lambda_h^* &= \max\{\lambda \mid \exists\, \boldsymbol{x} \in \mathcal{K}_d : \boldsymbol{A}\boldsymbol{x} = \lambda \boldsymbol{b}\} && (31)\\
&= \max_{\boldsymbol{x} \in \mathcal{K}_d} \min_{b^T y = 1} \boldsymbol{y}^T \boldsymbol{A} \boldsymbol{x} \\
&= \min_{b^T y = 1} \max_{\boldsymbol{x} \in \mathcal{K}_d} \boldsymbol{x}^T (\boldsymbol{A}^T \boldsymbol{y}) \\
&= \min_{b^T y = 1} D_d(\boldsymbol{y}). && (32)
\end{aligned}$$

The duality between (31) and (32) follows immediately from [9, Theorem 2.1], but is standard in the finite dimensional case.

From the discrete static form (31) it follows that $\lambda_h^* = 0$, if $\boldsymbol{b}$ does not belong to the range of $\boldsymbol{A}$, $R_A = \{\boldsymbol{A}\boldsymbol{x} \mid \boldsymbol{x} \in \mathbb{R}^N\}$. In order to handle general external forces we must impose the consistency condition $R_A = \mathbb{R}^M$ or, in other words, *the matrix $\boldsymbol{A}$ must have full row rank M*. In particular it is necessary that $N > M$. This is the compatibility condition on the space of discrete stresses $\boldsymbol{\sigma}_h$ mentioned above, and this is the reason why we must use piecewise bi–quadratic element functions for the components of $\boldsymbol{\sigma}_h$ instead of, e.g., piecewise bi–linear elements.

The use of piecewise bi–quadratic elements for $\boldsymbol{\sigma}_h$ introduces an error in connection with the yield condition. The inequality (20) imposes the yield condition (17) on $\boldsymbol{\sigma}_h$ only at the nodes. With bi–quadratic element functions it may be violated between nodes as indicated in Figure 1.

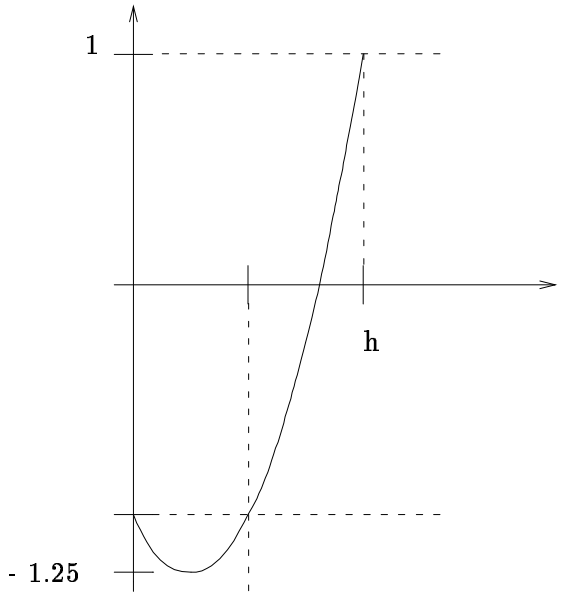

Figure 1: Constraint violation between nodes for a quadratic element function.

The maximum pointwise violation of the quadratic condition (17) may be as large as ca. 28% of the variation of a component of $\boldsymbol{\sigma}_h$ over the element. With a similar change of sign in the corresponding component of $\boldsymbol{\varepsilon}(\boldsymbol{u}_h)$ this may result in a value of $a(\boldsymbol{\sigma}_h, \boldsymbol{u}_h)$ which is too large. If we assume that the area where $\boldsymbol{\sigma}_h^*$ changes in such a "bang–bang" fashion decreases as $O(h)$, as h tends to zero, then the influence of the constraint violation on the discrete collapse multiplier λ_h^* will be $O(h)$ and thus can be considered part of the discretization error. In limit analysis we cannot expect faster convergence than $O(h)$ [10, 11, 14, 16].

We do not know to what extent the above constraint violation actually contributes to the discretization error in λ_h^*.

3 Solution of the discrete problem

We approach the discrete problem in the form (32). There is only one linear equality constraint, but the objective function (30) is not differentiable. The matrix $\boldsymbol{A}$ is sparse

with the usual finite element structure for problems in two space dimensions.

Using the notation (26) for the x–variables we have

$$\boldsymbol{x}^T \left(\boldsymbol{A}^T \boldsymbol{y}\right) = \sum_{\nu} \sum_{k=1}^{2} \xi_\nu^k \left(\boldsymbol{A}^T \boldsymbol{y}\right)_\nu^k .$$

Substituting for $\boldsymbol{x} \in \mathcal{K}_d$ in (30) the normalized yield condition (20), i.e.

$$\left(\xi_\nu^1\right)^2 + \left(\xi_\nu^2\right)^2 \leq 1 \quad \text{for all nodes} \quad \nu$$

we get

$$D_d(\boldsymbol{y}) = \sum_{\nu} \left(\left(\left(\boldsymbol{A}^T \boldsymbol{y}\right)_\nu^1 \right)^2 + \left(\left(\boldsymbol{A}^T \boldsymbol{y}\right)_\nu^2 \right)^2 \right)^{\frac{1}{2}} .$$

$D_d(\boldsymbol{y})$ is a sum of Euclidean norms of 2–dimensional vectors. Each term only involves two rows of $\boldsymbol{A}^T$, i.e. two columns of $\boldsymbol{A}$. These are precisely the two columns associated with the node ν, and they correspond to the value of the two components of $\boldsymbol{\sigma}_h$ at that node. Now let $\boldsymbol{A}_\nu$ denote the $M \times 2$ matrix consisting of these two columns, i.e. the two columns corresponding to the primal variables ξ_ν^1 and ξ_ν^2. Then we get the following expression for the objective function (30):

$$D_d(\boldsymbol{y}) = \sum_{\nu} \left(\left(\boldsymbol{A}_\nu^T \boldsymbol{y}\right)_1^2 + \left(\boldsymbol{A}_\nu^T \boldsymbol{y}\right)_2^2 \right)^{\frac{1}{2}} = \sum_{\nu} \left\| \boldsymbol{A}_\nu^T \boldsymbol{y} \right\| \tag{33}$$

The discrete problem (32) may now be written

$$\lambda_h^* = \min_{b^T y = 1} \sum_{\nu} \left\| \boldsymbol{A}_\nu^T \boldsymbol{y} \right\| \tag{34}$$

where the sum is over the nodes for the discrete stresses as explained above. In the optimal solution we typically expect a large number (in some applications more than 90%) of the terms in (34) to vanish and hence be non–differentiable. $D_d(\boldsymbol{y})$ defined by (30) is the discrete analogue of $D(\boldsymbol{u})$ defined by (12). Hence the nodes for which $\boldsymbol{A}_\nu^T \boldsymbol{y} = \boldsymbol{0}$ correspond to points where $\boldsymbol{\epsilon}(\boldsymbol{u}) = \boldsymbol{0}$, i.e. to points in the rigid region where there is no local deformation.

Calamai and Conn [6] and Overton [24] have developed second–order methods for problems like (34). The idea is to identify dynamically the zero–terms and then replace them by constraints of the type $\boldsymbol{A}_\nu^T \boldsymbol{y} = \boldsymbol{0}$. The code of Overton was applied to test problems in limit analysis in [25] and [21]. We started this work with a plan of modifying Overton's code for large sparse problems, but it turned out that a certain nondegeneracy condition discussed in [6, 21, 24, 25] is hard to handle in the general case. Results (for our application in the next section) with rather coarse grids were obtained in [14] with the

dense code, but we expect serious efficiency problems for finer grids. This motivated the development of a new algorithm by Andersen [4] based on the idea of barrier methods in linear programming. The results in the following section are obtained with this algorithm. We also find the dual solution, i.e. the stress field, and identify the nodes where the yield condition is satisfied with no slack. This is the plastified region.

4 The plate problem

Limit analysis for plastic plates is described in [8]. The variables are the three components of the bending moments m_{11}, m_{22} and $m_{12} = m_{21}$ and the transversal displacement rate u. The problem of limit analysis is formally the same as above with the following modifications:

$$\begin{aligned} a(\boldsymbol{m}, u) &= -\int_A \sum_{i,j=1}^{2} m_{ij} \frac{\partial^2 u}{\partial x_i \partial x_j}\, da \\ &= \int_A \left(\frac{\partial u}{\partial x_1} \left(\frac{\partial m_{11}}{\partial x_1} + \frac{\partial m_{12}}{\partial x_2} \right) + \frac{\partial u}{\partial x_2} \left(\frac{\partial m_{12}}{\partial x_1} + \frac{\partial m_{22}}{\partial x_2} \right) \right) da \qquad (35) \\ &= -\int_A u \left(\frac{\partial^2 m_{11}}{\partial x_1^2} + 2\frac{\partial^2 m_{12}}{\partial x_1 \partial x_2} + \frac{\partial^2 m_2}{\partial x_2^2} \right) da \\ F(u) &= \int_A f\ u\ da \qquad (36) \end{aligned}$$

where A denotes the area of the plate, and f is the transversal force. For computational purposes we always use the form (35) with one derivative on both $\boldsymbol{m}$ and u, so that standard finite element functions can be applied.

In the plate model the set of admissible moment tensors $\boldsymbol{m}$ is bounded. For example the Mises condition is in normalized form

$$m_{11}^2 - m_{11}m_{22} + m_{22}^2 + 3m_{12}^2 \le 1. \qquad (37)$$

Consequently $D(u)$ defined by

$$D(u) = \max_{m \in K} a(\boldsymbol{m}, u) \qquad (38)$$

is always finite.

With the substitutions (35), (36) and (37) the problem of limit analysis is formally the same as discussed above. The discretization is much simpler in the plate model because the energy dissipation rate $D(u)$ is finite for all u, so that standard finite element spaces may be used. As in [17] we use piecewise bi–linear element functions for both u and the

components of $\boldsymbol{m}$, but piecewise linear elements over triangles would do just as well. The nodes are the vertices of the rectangles, and the nodal values are the values of m_{11}, m_{22}, m_{12} and u at the vertices.

The discrete moment tensor may be written

$$\boldsymbol{m}_h = \sum_\nu \left(\xi_\nu^{11} \boldsymbol{\varphi}_\nu^{11} + \xi_\nu^{22} \boldsymbol{\varphi}_\nu^{22} + \xi_\nu^{12} \boldsymbol{\varphi}_\nu^{12} \right) \tag{39}$$

where

$$\boldsymbol{\varphi}_\nu^{11} = \begin{bmatrix} \varphi_\nu & 0 \\ 0 & 0 \end{bmatrix}, \quad \boldsymbol{\varphi}_\nu^{22} = \begin{bmatrix} 0 & 0 \\ 0 & \varphi_\nu \end{bmatrix}, \quad \boldsymbol{\varphi}_\nu^{12} = \begin{bmatrix} 0 & \varphi_\nu \\ \varphi_\nu & 0 \end{bmatrix} \tag{40}$$

φ_ν denotes the scalar bi–linear element function equal to one at the node ν and zero at all other nodes. The yield condition is again imposed through the nodal values:

$$\left(\xi_\nu^{11}\right)^2 - \xi_\nu^{11} \xi_\nu^{22} + \left(\xi_\nu^{22}\right)^2 + 3 \left(\xi_\nu^{12}\right)^2 \leq 1$$

or equivalently

$$\boldsymbol{\xi}_\nu^T \boldsymbol{Q} \boldsymbol{\xi}_\nu \leq 1 \quad \text{for all nodes } \nu, \tag{41}$$

where

$$\boldsymbol{Q} = \begin{bmatrix} 1 & -\frac{1}{2} & 0 \\ -\frac{1}{2} & 1 & 0 \\ 0 & 0 & 3 \end{bmatrix}, \quad \boldsymbol{\xi}_\nu = \begin{bmatrix} \xi_\nu^{11} \\ \xi_\nu^{22} \\ \xi_\nu^{12} \end{bmatrix}. \tag{42}$$

With piecewise bi–linear elements the yield condition will be satisfied at every point if it is satisfied at the nodal points.

The discrete transversal flow is a scalar function:

$$u_h = \sum_\mu \eta_\mu \, \psi_\mu, \tag{43}$$

where $\psi_\mu = \varphi_\mu$ are the same scalar functions as for the moments.

In analogy with (21) and (23) we get

$$F(u_h) = \sum_\mu \eta_\mu \, F(\psi_\mu) \tag{44}$$

and

$$a(\boldsymbol{m}_h, u_h) = \sum_\nu \sum_\mu \left(\xi_\nu^{11} \eta_\mu a\left(\boldsymbol{\varphi}_\nu^{11}, \psi_\mu\right) + \xi_\nu^{22} \eta_\mu a\left(\boldsymbol{\varphi}_\nu^{22}, \psi_\mu\right) + \xi_\nu^{12} \eta_\mu a\left(\boldsymbol{\varphi}_\nu^{12}, \psi_\mu\right) \right) \tag{45}$$

with

$$\begin{aligned} a\left(\boldsymbol{\varphi}_\nu^{11},\psi_\mu\right) &= \int_A \frac{\partial\varphi_\nu}{\partial x_1}\frac{\partial\psi_\mu}{\partial x_1}\,da \\ a\left(\boldsymbol{\varphi}_\nu^{22},\psi_\mu\right) &= \int_A \frac{\partial\varphi_\nu}{\varphi x_2}\frac{\partial\psi_\mu}{\partial x_2}\,da \\ a\left(\boldsymbol{\varphi}_\nu^{12},\psi_\mu\right) &= \int_A \left(\frac{\partial\varphi_\nu}{\partial x_2}\,\frac{\partial\psi_\mu}{\partial x_1}+\frac{\partial\varphi_\nu}{\partial x_1}\,\frac{\partial\psi_\mu}{\partial x_2}\right)da. \end{aligned}$$

Again we introduce linear numberings

$$\begin{aligned} n &= n(\nu,i,j)\in\{1,\cdots,N\}\ , \quad x_n=\xi_\nu^{ij} \\ m &= m(\mu)\in\{1,\cdots,M\}\ , \quad y_m=\eta_\mu \end{aligned}$$

and obtain

$$F(u_h)=\sum_{m=1}^{M} y_m\ b_m=\boldsymbol{b}^T\boldsymbol{y} \tag{46}$$

with

$$b_m=F(\psi_\mu) \quad \text{for} \quad m=m(\mu)$$

and

$$a(\boldsymbol{m}_h,u_h)=\sum_{m=1}^{M}\sum_{n=1}^{N} y_m x_n a_{mn}=\boldsymbol{y}^T\boldsymbol{A}\boldsymbol{x}=\boldsymbol{x}^T\left(\boldsymbol{A}^T\boldsymbol{y}\right) \tag{47}$$

with

$$a_{mn}=a\left(\boldsymbol{\varphi}_\nu^{ij},\psi_\mu\right) \quad \text{for} \quad n=n(\nu,i,j),\ m=m(\mu).$$

The component of $\boldsymbol{A}^T\boldsymbol{y}$ corresponding to $n=n(\nu,i,j)$ is

$$\left(\boldsymbol{A}^T\boldsymbol{y}\right)_\nu^{ij}=\sum_\mu\ a\left(\boldsymbol{\varphi}_\nu^{ij},\psi_\mu\right)\eta_\mu.$$

Hence (47) may be written

$$\boldsymbol{x}^T\left(\boldsymbol{A}^T\boldsymbol{y}\right)=\sum_\nu\left(\xi_\nu^{11}\left(\boldsymbol{A}^T\boldsymbol{y}\right)_\nu^{11}+\xi_\nu^{22}\left(\boldsymbol{A}^T\boldsymbol{y}\right)_\nu^{22}+\xi_\nu^{12}\left(\boldsymbol{A}^T\boldsymbol{y}\right)_\nu^{12}\right). \tag{48}$$

Now let $\boldsymbol{A}_\nu$ denote the $M\times 3$ matrix consisting of the three columns from $\boldsymbol{A}$ associated with the node ν. With the notation (42) we get

$$\begin{aligned} D_d(\boldsymbol{y}) &= \max_{\xi_\nu^T Q\xi_\nu\le 1}\sum_\nu \boldsymbol{\xi}_\nu^T\left(\boldsymbol{A}_\nu^T\boldsymbol{y}\right) \\ &= \sum_\nu \max_{\xi_\nu^T Q\xi_\nu\le 1}\boldsymbol{\xi}_\nu^T\left(\boldsymbol{A}_\nu^T\boldsymbol{y}\right) \\ &= \sum_\nu\left(\left(\boldsymbol{A}_\nu^T\boldsymbol{y}\right)^T\boldsymbol{Q}^{-1}\left(\boldsymbol{A}_\nu^T\boldsymbol{y}\right)\right)^{\frac{1}{2}} \\ &= \sum_\nu\left\|\boldsymbol{C}^T\left(\boldsymbol{A}_\nu^T\boldsymbol{y}\right)\right\| \end{aligned}$$

where $\boldsymbol{C}$ is the Cholesky factor of Q^{-1} :

$$\boldsymbol{C} = \frac{1}{\sqrt{3}} \begin{bmatrix} 2 & 0 & 0 \\ 1 & \sqrt{3} & 0 \\ 0 & 0 & 1 \end{bmatrix}.$$

The discrete problem for plates analogous to (34) is then

$$\lambda_h^* = \min_{b^T y = 1} \sum_{\nu} \left\| (\boldsymbol{A}_\nu \boldsymbol{C})^T \boldsymbol{y} \right\|. \tag{49}$$

This is again the minimization of a sum of norms, and the algorithms discussed in the previous section apply.

In general, quadratic yield conditions give rise to problems of the form (49). The $\boldsymbol{A}_\nu$ are columns of the equilibrium matrix $\boldsymbol{A}$, while $\boldsymbol{C}$ depends only on the yield condition.

5 Computational results

The method is applied to solve problems in two plane models: plane strain and plates. In the computations reported here uniform grids are used. Adaptive mesh generation can and should be used, but our main goal is to demonstrate the strength of the discretization and the optimization algorithm.

We first apply the method in Section 3 to the test problem in plane strain described in [5, 10, 16] and [14, Example 11.1]. A rectangular block with thin symmetric cuts is being pulled by a uniform tensile force at the end faces. Figure 2 shows a cross section of the block, and the reduction of the problem size by symmetry.

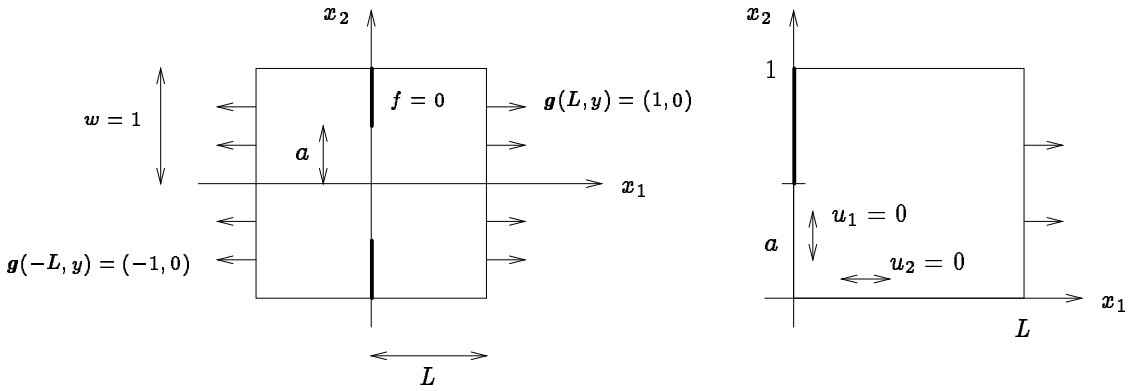

Figure 2: Geometry of the test problem in plane strain

When comparing with other results we focus on the obtainable mesh size (which determines the discretization error) and on the quality of the computed collapse fields for stresses and flow. In [5] the yield condition was linearized and the resulting LP was solved, using a 200×200 grid. In [14, section 13] the convex problem (32) was solved directly on a 30×30 grid applying MINOS [23] to the static formulation, but with poorly determined stresses. In both cases piecewise constant elements were used for the stresses and piecewise bi–linear elements for the flow.

In comparison, the largest problem solved with our new method is for a 120×120 grid. However, since the elements of higher degree used here provide four times as many degrees of freedom per node, a 120×120 grid corresponds in accuracy and problem size to a 240×240 grid in [5] and [14, Section 13].

	$a = 1/3$			$a = 1/2$			$a = 2/3$		
h^{-1}	$\lambda^*(h)$	$k(h)$	$R(h)$	$\lambda^*(h)$	$k(h)$	$R(h)$	$\lambda^*(h)$	$k(h)$	$R(h)$
6	0.9898			1.2193			1.4775		
12	0.9560		0.9221	1.1751		1.1308	1.4336		1.3896
18	0.9450	1.05	0.9230	1.1603	1.00	1.1309	1.4172	0.80	1.3844
24	0.9396	1.06	0.9235	1.1530	1.02	1.1311	1.4088	0.95	1.3838
30	0.9364	1.05	0.9237	1.1487	1.03	1.1313	1.4038	0.95	1.3835
36	0.9343	1.05	0.9238	1.1458	1.02	1.1314	1.4003	0.97	1.3833
42	0.9328	1.05	0.9239	1.1437	1.02	1.1314	1.3979	0.97	1.3832
48	0.9317	1.04	0.9239	1.1422	1.02	1.1314	1.3961	0.98	1.3832
54	0.9308	1.05	0.9240	1.1410	1.01	1.1315	1.3946	0.99	1.3832
60	0.9302	1.04	0.9240	1.1401	1.02	1.1315	1.3935	0.99	1.3831
90	0.9281	1.04	0.9241	1.1372	1.01	1.1315	1.3900	0.99	1.3831
99	0.9278	1.03	0.9241				1.3894	0.99	1.3831
100				1.1366	1.01	1.1315			
120	0.9271	1.03	0.9241						

Table 1: Results and convergence analysis for the test problem in Figure 2, $L = 1$, $a = \frac{1}{3}$, $a = \frac{1}{2}$ and $a = \frac{2}{3}$. $k(h)$ is the computed convergence order, and $R(h)$ the Richardson extrapolation to order 1.

A selection of our results is shown in Table 1 and visualized in comparison with the results from [5] and [14, Section 13] in Figure 3. We can solve the convex problem (32)

at least as accurately as the LP solved in [5], even ignoring the linearization error which is about 2%.

Table 1 shows, for $L = 1$ and the cases $a = \frac{1}{3}$, $a = \frac{1}{2}$ and $a = \frac{2}{3}$ (see Figure 2), some computed values for λ_h^*, the estimated convergence order based on these values (as described in [18]), and the estimate of λ^* obtained by Richardson extrapolation to order $k = 1$. These values are computed from the expression

$$R(h_i) = \frac{\alpha^k \lambda^*(h_i) - \lambda^*(h_{i-1})}{\alpha^k - 1}, \quad \alpha = \frac{h_{i-1}}{h_i}$$

where $h_i < h_{i-1}$ are 2 successive h-values in the table. The convergence analysis shows that the collapse multiplier λ_h^* converges in h with order 1, in the sense that the limit

$$\lim_{h \to 0} \frac{1}{h}(\lambda_h^* - \lambda^*) \tag{50}$$

exists. This was found not to be the case in [5] where the expression in (50) was bounded, but not convergent, as $h \to 0$. The explanation is that the finite element functions of higher degree used here approximate even the non–smooth collapse fields in limit analysis better than piecewise linear or bi–linear elements, although the convergence order is still $k = 1$. This makes it possible to estimate the discretization error and extrapolate to obtain an accuracy not seen before in limit analysis. For example we claim that in the case $L = 1$ and $a = \frac{1}{3}$ we have $\lambda^* = 0.9241$ with all digits correct.

Figure 4 visualizes the computed collapse fields $\boldsymbol{u}_h^*$ and $\boldsymbol{\sigma}_h^*$ for the case $L = 1$, $a = \frac{1}{3}$, $h = \frac{1}{120}$. As is standard, we have multiplied the displacement rate $\boldsymbol{u}_h^*$ by a suitable time–scale in order to see the resulting deformation. The deformed grid is not necessarily linear between nodes due to the higher order element functions. Rigid regions separated by a narrow slip zone are clearly recognizable. The nodes in the rigid region correspond to zero–norms in the sum (34). The nodes where the stress tensor satisfies the yield condition without slack are indicated by a small line segment indicating the direction of the vector (σ_1, σ_2) in (16). These nodes make up the plastified region. On this fine grid the direction can hardly be recognized, but the plastified region is clearly visible. In Figures 4 and 5, a node is considered plastified if the slack in the yield condition is less than 10^{-8}, but the picture is almost the same for all tolerances between 10^{-10} and 10^{-6}. The collapse fields are in agreement with those found in [5], but slightly better determined.

Figure 5 shows the collapse solution for the case $L = 2$, $a = \frac{1}{3}$, $h = \frac{1}{60}$. We see that the plastified region does not penetrate to the side $x = L$, suggesting that the collapse solution, in particular the limit multiplier λ^*, should remain the same if material is added

to the rightmost rigid block. This was confirmed by actually computing the collapse solution for $L = 3$. For $h = \frac{1}{3}$ the values of λ_h^* for $L = 2$ and $L = 3$ are 1.258833 and 1.259579, respectively, but for $h \leq \frac{1}{12}$ the values of λ_h^* for $L = 2$ and $L = 3$ are identical. Through the same analysis as in Table 1 we find that for $L \geq 2$ and $a = \frac{1}{3}$ the limit multiplier is $\lambda^* = 1.130 \pm 0.001$.

The discrete problem corresponding to Figure 4 (the largest case solved) has $M = 58240$ variables (u–components) and $N = 116162$ dual variables (σ–components). There are 58081 terms in the sum (34) out of which more than 80% are zero in the optimal solution. The matrix $\boldsymbol{A}$ has $2,092,843$ nonzero elements. The computation used 79 hours of CPU–time on the CONVEX C3240 vector computer at Odense University. The accuracy measured in duality gap and lack of feasibility is about 10^{-8}. The CPU–time is considerable, but we have tried to test the limits of the method. In our experience the bottleneck in limit analysis has not been the CPU–time or storage, but the deterioration of accuracy due to ill conditioning. In this respect the present method is beyond comparison.

The second application is the plate bending problem described in [17]: Various combinations of simply supported/clamped, square/rectangular plates loaded by a uniform load or a point load at the center. In [17] results are reported for meshes up to 40×40 grids on the square plate (reduced to 20×20 by symmetry). We have results for 800×800 grids (reduced to 400×400 by symmetry). As in [17] piecewise bilinear finite element functions are used both for u and for the components of $\boldsymbol{m}$.

The largest case solved has $M = 160000$ variables, $N = 482403$ dual variables, 160801 terms in the sum (34), and the matrix $\boldsymbol{A}$ has 3,390,400 nonzero entries. The computation used 5.7 hours of CPU–time (same computer as above). The duality gap was less than 10^{-8}, while infeasibilities (primal and dual) were less than 10^{-10}. This problem can be solved very efficiently because all terms in the sum of norms (34) are nonzero in the optimal solution. This was also essential for the results in [17] which were obtained using the smooth optimization algorithm by Goldfarb [22].

Our results agree with earlier results, but the fact that we are able to solve for much finer grids makes a better convergence analysis possible. This is done as described in [18]. Table 2 shows the value of λ_h^* for the simply supported square plate with uniform load. The computed convergence orders $k_1(h)$ in column 3 confirm that the error is of order 2. Column 4 shows the result $R_1(h)$ of Richardson extrapolation to order 2. We then estimate the order $k_2(h)$ of the error after extrapolation (column 5) and find the order 3.

h^{-1}	$\lambda(h)$	$k_1(h)$	$R_1(h)$	$k_2(h)$	$R_2(h)$
12	24.86336954				
24	24.97645373		25.01414846		
36	24.99948059	1.84	25.01790208		25.01884048
48	25.00787151	1.89	25.01865984	2.56	25.01908081
60	25.01183455	1.92	25.01887995	3.06	25.01907256
72	25.01401352	1.94	25.01896572	3.09	25.01906865
84	25.01533804	1.95	25.01900594	3.06	25.01906738
96	25.01620269	1.96	25.01902721	3.07	25.01906672
108	25.01679808	1.97	25.01903955	3.03	25.01906653
120	25.01722540	1.97	25.01904713	3.09	25.01906623
200	25.01839885	1.98	25.01905892	2.99	25.01906628
300	25.01876857	1.98	25.01906435	3.03	25.01906621
400	25.01889849	1.99	25.01906553	3.03	25.01906619

Table 2: Results and convergence analysis for the simply supported, uniformly loaded square plate.

2 and 3 are the expected orders of the two lowest order terms for smooth solutions u^* and $\boldsymbol{m}^*$ with piecewise bilinear element functions. Finally column 6 shows the result $R_2(h)$ of a second extrapolation, this time to order 3. For this case we get $\lambda^* = 25.019066$ with all digits correct.

For the uniformly loaded clamped plate the results are shown in Table 3. In the clamped case u^* has a singularity in the form of a so-called hinge along the boundary, resulting in a slower convergence. An analysis similar to the one for Table 2 indicates that the lowest two orders in the error are 1.5 and 2. For this case we find the value $\lambda^* = 44.1269$ with uncertainty in the last digit only. This confirms the value found in [17, page 180], but is in conflict with a conjecture in [1, page 135], which implies a lower bound of 44.46. This discrepancy cannot possibly be explained by the discretization error. The computer programs used in the present work and in [17] were prepared completely independently, although both are based on the same conceptual method for discretizing the clamped plate by the finite element method. In [1, page 135] the authors agree that "the computed results throw doubt on the validity of the conjecture". From our results we draw the conclusion that the conjecture is incorrect.

h^{-1}	$\lambda(h)$	$k_1(h)$	$R_1(h)$	$k_2(h)$	$R_2(h)$
24	43.73575159				
36	43.91239918		44.12341810		
48	43.98660561	1.49	44.12412661		44.12484481
60	44.02590034	1.48	44.12474444	-0.52	44.12567757
72	44.04966063	1.48	44.12520184	0.33	44.12612043
96	44.07627631	1.48	44.12560108	1.38	44.12625923
120	44.09041730	1.47	44.12598832	0.31	44.12657317
200	44.10973000	1.46	44.12649948	0.49	44.12695585
400	44.12076200	1.47	44.12679560	2.20	44.12691930
800	44.12471300	1.48	44.12687387	2.28	44.12689996

Table 3: Results and convergence analysis for the clamped, uniformly loaded square plate.

The collapse multiplier λ_h^* for a discrete point load is shown in Figure 6 for the following four cases: Simply supported/clamped and square (1×1)/rectangular (1×2) plate. In the clamped case the values for the square and rectangular plate (white and black diamonds in Figure 6) overlap almost completely, and the difference tends to zero with h. In the plastic plate model a point load is only admissible as a limit of concentrated loads and may be approximated by a sequence of discrete loads "shrinking" with h as well as by discrete point loads. (For details see [17, page181].) Since the error in the simply supported case is quite large (white and black circles in Figure 6), we have also approximated the point load by a sequence of unit loads distributed uniformly on a central square of side h (white squares in Figure 6). As mentioned in [17] this approximation must yield the same limit as the discrete point loads if the concept of a point load is valid. This appears to be the case.

Our results confirm (although not beyond any doubt) a claim made in [17]: The 5 sequences of discrete values λ_h^* in Figure 6 converge to the same limit. This means that the limit multiplier for a point load does not depend on shape or support of the plate. We find this value to be $\lambda^* = 6.82 \pm 0.01$.

Convergence analysis shows that for all the above mentioned discretizations λ_h^* converges more slowly than h^k for any power $k > 0$, as $h \to 0$. The collapse solutions in Figure 7 (simply supported plate) and Figure 8 (clamped plate) clearly indicate why: The

deformation is singular. On the other hand, our results indicate that the deformation converges as $h \to 0$, which means that the peak at the center is finite. The solutions shown in Figure 7 and 8 are for a 200×200 grid (by symmetry the computation is reduced to a 100×100 grid). The largest case solved is for an 800×800 grid, but this is too fine to plot.

References

[1] J. D. Allen, I. F. Collins, and P. G. Lowe, *Limit analysis of plates and isoperimetric inequalities*, Philos. Trans. Roy. Soc. London Ser. A, 347 (1994), pp. 113–137.

[2] E. Anderheggen and H. Knöpfel, *Finite element limit analysis using linear programming*, Internat. J. Solids and Structures, 8 (1972), pp. 1413–1431.

[3] K. D. Andersen, *An infeasible dual affine scaling method for linear programming*, Committee on Algorithms Bulletin (COAL), 22 (1993), pp. 20–28.

[4] ——, *An efficient Newton barrier method for minimizing a sum of Euclidean norms*, SIAM J. Optim, (1995). To appear.

[5] K. D. Andersen and E. Christiansen, *Limit analysis with the dual affine scaling algorithm*, J. Comput. Appl. Math., (1994). To appear.

[6] P. H. Calamai and A. R. Conn, *A second order method for solving the continuous multifacility location problem*, in Numerical Analysis: Proceedings of the Ninth Biennial Conference in Dundee, G. A. Watson, ed., vol. 912 of Lecture Notes in Mathematics, Springer Verlag, Berlin, 1982, pp. 1–25.

[7] M. Capurso, *Limit analysis of continuous media with piecewise linear yield condition*, Meccanica—J. Ital. Assoc. Theoret. Appl. Mech., 6 (1971), pp. 53–58.

[8] E. Christiansen, *Limit analysis for plastic plates*, SIAM J. Math. Anal., 11 (1980), pp. 514–522.

[9] ——, *Limit analysis in plasticity as a mathematical programming problem*, Calcolo, 17 (1980), pp. 41–65.

[10] ——, *Computation of limit loads*, Internat. J. Numer. Methods Engrg., 17 (1981), pp. 1547–1570.

[11] ——, *Examples of collapse solutions in limit analysis*, Utilitas Math., 22 (1982), pp. 77–102.

[12] ——, *On the collapse solution in limit analysis*, Arch. Rational Mech. Anal., 91 (1986), pp. 119–135.

[13] ——, *Limit analysis with unbounded convex yield condition*, in IMACS '91: Proceedings of the 13th World Congress on Computation and Applied Mathematics, R. Vichnevetsky and J. J. H. Miller, eds., Criterion Press, Dublin, 1991, pp. 129–130.

[14] ——, *Limit analysis of collapse states*, in Handbook of Numerical Analysis, P. G. Ciarlet and J. L. Lions, eds., vol. 4, North-Holland, Amsterdam, 1994.

[15] E. Christiansen and K. O. Kortanek, *Computing material collapse displacement fields on a CRAY X-MP/48 by the primal affine scaling algorithm*, Ann. Oper. Res., 22 (1990), pp. 355–376.

[16] ——, *Computation of the collapse state in limit analysis using the LP primal affine scaling algorithm*, J. Comput. Appl. Math., 34 (1991), pp. 47–63.

[17] E. Christiansen and S. Larsen, *Computations in limit analysis for plastic plates*, Internat. J. Numer. Methods Engrg., 19 (1983), pp. 169–184.

[18] E. Christiansen and H. G. Petersen, *Estimation of convergence orders in repeated Richardson extrapolation*, BIT, 29 (1989), pp. 48–59.

[19] P. G. Ciarlet, *The Finite Element Method for Elliptic Problems*, North-Holland, Amsterdam, 1978.

[20] ——, *Basic error estimates for elliptic problems*, in Handbook of Numerical Analysis, P. G. Ciarlet and J. L. Lions, eds., vol. 2, North-Holland, Amsterdam, 1991.

[21] V. F. Gaudrat, *A Newton type algorithm for plastic limit analysis*, Comput. Methods Appl. Mech. Engrg., 88 (1991), pp. 207–224.

[22] D. Goldfarb, *Extension of Davidon's variable metric method to maximization under linear inequality and equality constraints*, SIAM J. Appl. Math., 17 (1969), pp. 739–764.

[23] B. A. Murtagh and M. A. Saunders, *A projected lagrangian algorithm and its implementation for sparse nonlinear constraints*, in Algorithms for Constrained Minimization of Smooth Nonlinear Functions, A. G. Buckley and J.-L. Goffin, eds., vol. 16 of Mathematical Programming Study, North-Holland, Amsterdam, 1982, pp. 84–117.

[24] M. L. Overton, *A quadratically convergent method for minimizing a sum of Euclidean norms*, Math. Programming, 27 (1983), pp. 34–63.

[25] ——, *Numerical solution of a model problem from collapse load analysis*, in Proceedings of the Sixth International Symposium on Computer Methods in Engineering and Applied Sciences, R. Glowinski and J. L. Lions, eds., Institut National de Recherche en Informatique et en Automatique (Versailles, France), North-Holland, Amsterdam, 1984, pp. 421–437.

[26] R. Temam, *Navier-Stokes Equations*, North-Holland, Amsterdam, 1977.

Caption for Figure 3

Computed values of the collapse multiplier for the test problem in Figure 2:

$+$: Exact yield condition, divergence-free elements (new results).

$\times$: Exact yield condition, constant-bilinear elements (from [14, Section 13]).

$\triangledown$: Linearized yield condition, constant-bilinear elements (from [5]).

Figure 3: Caption on opposite page.

Figure 4: Collapse fields for the test problem in Figure 2: $L = 1$, $a = \frac{1}{3}$, $h = \frac{1}{120}$.

Figure 5: Collapse fields for the test problem in Figure 2: $L = 2$, $a = \frac{1}{3}$, $h = \frac{1}{60}$.

Caption for Figure 6

Computed values of the collapse multiplier for various approximations of a point load:

$\circ$: Simply supported square plate; discrete point load.

$\bullet$: Simply supported rectangular plate; discrete point load.

$\diamond$: Clamped square plate; discrete point load.

$\blacklozenge$: Clamped rectangular plate; discrete point load.

$\square$: Simply supported square plate; load concentrated uniformly at a central square of side h.

Figure 6: Caption on opposite page.

Figure 7: Simply supported square plate with point load.

Figure 8: Clamped square plate with point load.